

Line-of-sight gas radiation effects on near-infrared two-color ratio pyrometry measurements during plasma wind tunnel experiments

Andrea Fagnani^{a,b,*}, Bernd Helber^a, Annick Hubin^b, Olivier Chazot^a

^a*Aeronautics and Aerospace Department, von Karman Institute for Fluid Dynamics, Chaussée de Waterloo, 72, Rhode-st-Genèse, 1640, Belgium*

^b*Materials and Chemistry Department, Vrije Universiteit Brussel, Pleinlaan, 2, Brussel, 1150, Belgium*

Abstract

Two-color ratio pyrometry is commonly used to measure the surface temperature of aerospace materials during plasma wind tunnel experiments. However, the effect of the plasma radiation on the measurement accuracy is often neglected. In this paper we formulate a model of the instrument response to analyze the systematic error induced by the gas radiation along the optical path. CFD simulations of the plasma flow field, together with a radiation code, allow to compute the gas spectral radiance within the instrument wavelength range. The measurement error is numerically assessed as a function of the true object temperature and emittance value. Our simulations explain the typical behavior observed in experiments, showing that a significant bias can affect the measured temperature during the material heating phase. For an actual experiment on a ceramic-matrix composite, a correction to the measured data is proposed, while comparative measurements with a spectrometer corroborate the results.

Keywords:

Two-color pyrometry, Error analysis, Gas emission, Plasma wind tunnels, Thermal Protection Materials

1. Introduction

The hypersonic flight of a spacecraft through a planetary atmosphere is a fascinating engineering endeavor, often representing the most critical part of a

*Corresponding author

Email addresses: andrea.fagnani@vki.ac.be (Andrea Fagnani), bernd.helber@vki.ac.be (Bernd Helber), annick.hubin@vub.be (Annick Hubin), olivier.chazot@vki.ac.be (Olivier Chazot)

space mission. During atmospheric entry, the vehicle’s kinetic energy is converted into thermal energy of the flow across a strong shock wave, creating an extreme aero-thermal environment [1]. Gas temperatures can rise above 10000 K, thus producing a chemically-reacting plasma flow. Thermal Protection Systems (TPSs) are designed to shield the spacecraft from the severe heat loads [2], ensuring safety of the crew and payload onboard. In this context, Plasma Wind Tunnels (PWTs) offer a laboratory testing environment that allows to study complex gas-surface interaction phenomena, resulting from the TPS material response to high-temperature chemically-reacting flows [3]. These facilities typically use arc heaters or Inductively Coupled Plasma (ICP) torches to produce a high-temperature plasma jet, which is impinged onto a test material sample to duplicate a real flight scenario [4].

In the context of PWT experiments, InfraRed (IR) radiometry is commonly used to characterize the material response during exposure to the plasma jet [5], as it allows non-intrusive probing of the surface temperature up to extreme values (~ 3000 K). In particular, multi-spectral radiometry is a class of IR techniques that offers some key advantages. Single band IR measurements, in fact, require prior knowledge of the material’s emittance to correct the measured signal in order to retrieve the target temperature [6]. Multi-spectral systems, instead, provide simultaneous measurements of the object irradiance in N wavelength bands. By making suitable assumptions on the behavior of the spectral emittance, ε_λ , the system of measurement equations can be solved for the object temperature and the $N - 1$ parameters describing ε_λ [7–9]. As a result, these techniques allow measuring the material’s surface temperature even when its emittance is unknown or changing in an unpredictable fashion, which represents a key factor for PWT metrology [10].

Two-Color Pyrometry (TCP) is the simplest case of multi-spectral radiometry, employing only two measurements bands, and it is therefore widely employed to monitor the evolution of the material surface temperature during PWT experiments [5, 10–16]. Recently, some authors have proposed advanced applications, including two-color imaging pyrometry using CCD cameras [17, 18], two-color thermographic imaging using IR cameras [19–21] and high-speed three-dimensional tomographic two-color pyrometry of flames [22]. Although one parameter can be used to model ε_λ in TCP, it is common practice to assume a uniform behavior (gray-body) in the wavelength range of interest. As a result, the ratio of the measured signals becomes independent of the emittance, allowing to solve directly for the object temperature (two-color ratio pyrometry) [7]. In this case, the sensitive wavelength bands are typically selected very close to each other to reduce the approximation error (local gray-body assumption). This, however, increases the sensitivity of the signal ratio to noise and effects of participating media along the optical path, as well as to any variation of ε_λ , should it occur [23]. Accurate

selection of the wavelength bands, in terms of range and spacing, determines the sensitivity of the instrument to a change in temperature of the emitting source [24]. For values between 500 K and 2500 K, such as those typically encountered on materials during PWT experiments, the highest sensitivity is obtained around 1 μm . This range is also weakly affected by optical path absorption from CO_2 and H_2O [25], making it ideal for calibration purposes.

The effects on TCP related to the gray-body assumption, in case of a real surface with variable spectral emittance [19, 26], as well as to environmental factors, in terms of ambient reflections [27, 28], window transmission [29] or absorption along the optical path [25, 30], as well as background radiation [31], have received considerable attention in the literature. However, the influence of gas radiation in PWT metrology is often neglected. In this case, the plasma jet, reaching temperatures within 5000-10 000 K, produces an intense emission along the optical path between the instrument and the material's surface. This primarily originates from the spontaneous emission of excited atoms and molecules in the ultraviolet (UV) to near-infrared (NIR) wavelength region of the electromagnetic spectrum [32, 33]. As this overlaps with the wavelength range of many commercial two-color pyrometers, we can expect the plasma emission to induce systematic errors on the measured temperature.

Notably, Loesener and co-workers [34, 35] already considered this source of interference; the problem, however, was chiefly avoided either selecting a suitable spectral region where the gas radiation was weak enough, or measuring the temperature of the material on the back surface, in order to avoid the pyrometer optical path to cross the plasma jet. MacDonalds et al. [36] also conducted a preliminary analysis of the error induced by the plasma radiation from an ICP torch on a single-band IR pyrometer. The problem was treated more extensively in the context of plasma-sprayed particle diagnostics, where some researchers analyzed the influence of both direct plasma emission and scattered light on the measurement of the particle temperature by means of TCP. For instance, Sakuta and Boulos [37] defined a thermal visibility factor, based on the ratio of the particle emission to the sum of particle and gas emission along the line of sight. A critical plasma temperature could be identified, depending on the particle surface temperature and emittance value, defining an acceptable measurement range. Gougeon and Moreau [38] investigated the influence of the scattered light by combining spectroscopic measurements and the Mie scattering theory. They showed that large positive errors could affect the measured temperature, as later confirmed by Salhi et al. [39]. Correspondingly, a minimum measurable temperature could be defined as a function of the plasma emission intensity. More recently, Aziz et al. [40] measured the spectral signature of an Ar/He plasma loaded with zirconia particles, also concluding that TCP measurements could be significantly affected by the plasma emission along the line of sight.

Starting from these considerations, we propose to study the effect of the plasma emission along the optical path on TCP measurements during PWT experiments of TPS materials. Our approach is based on a model for the response of a two-color ratio pyrometer (sec. 2), which, after calibration (sec. 3), allows to compute the effect of the gas radiation on the measured temperature. Starting from CFD simulations of the flow field, the plasma emission along the line of sight is numerically simulated with a radiation code. The effect on the measured temperature is studied as a function of the ICP torch electric power, as well as in terms of the material surface temperature and emittance value (sec. 4), showing that a large positive bias can be expected during the transient heating phase of the material sample. Experimental results on a ceramic matrix composite (sec. 5), tested in the Plasmatron facility at the von Karman Institute for Fluid Dynamics (VKI), confirm the predicted trends. A correction to the measured signals allows to compensate for the biasing effect, while a comparative analysis with a spectrometer, simultaneously probing the line-of-sight emission, corroborates the results.

2. TCP Instrument Response Model

Let us consider an IR instrument with absolute spectral radiance responsivity $R_\lambda = k\tilde{R}_\lambda$ [A W⁻¹], which includes detector sensitivity and internal optics transmission, where \tilde{R}_λ is the normalized spectral response and k is the absolute sensitivity coefficient. Then, the radiometric measurement equation relates the instrument output signal, S , to the spectral radiance incident on the instrument collector optics, L_λ , as [41, 42]

$$S = \Theta k \int_{\Delta\lambda} \tilde{R}_\lambda L_\lambda d\lambda \quad [\text{A}], \quad (1)$$

where Θ [m² sr] is the instrument optical throughput, λ is the wavelength and $\Delta\lambda$ is the range defined by \tilde{R}_λ . Then, the signal S is digitalized by the instrument electronics and recorded through a software interface.

Neglecting ambient reflections and optics emission for the high object temperatures of our application ($T_{\text{obj}} > 500$ K), considering the schematic in Fig. 1, L_λ can be written as

$$L_\lambda \cong \tau_\lambda^{\text{atm}} \tau_\lambda^{\text{win}} \varepsilon_\lambda L_\lambda^{\text{bb}}(T_{\text{obj}}) + \tau_\lambda^{\text{win}} L_\lambda^{\text{g,e}} + \tau_\lambda^{\text{atm}} \tau_\lambda^{\text{win}} (1 - \varepsilon_\lambda) L_\lambda^{\text{g,s}} \quad [\text{W m}^{-2} \text{sr}^{-1} \mu\text{m}^{-1}]. \quad (2)$$

Here, $\tau_\lambda^{\text{atm}}$ and $\tau_\lambda^{\text{win}}$ represent the spectral transmittance of the atmosphere and external optics along the optical path, respectively, while ε_λ is the spectral directional emittance of the material's surface. $L_\lambda^{\text{bb}}(T_{\text{obj}})$ is the spectral radiance of an ideal blackbody at temperature T_{obj} , described by Planck's law as [43]

$$L_\lambda^{\text{bb}}(\lambda, T) = \frac{2hc}{\lambda^5} \frac{1}{\exp[hc/(k_B\lambda T)] - 1}, \quad (3)$$

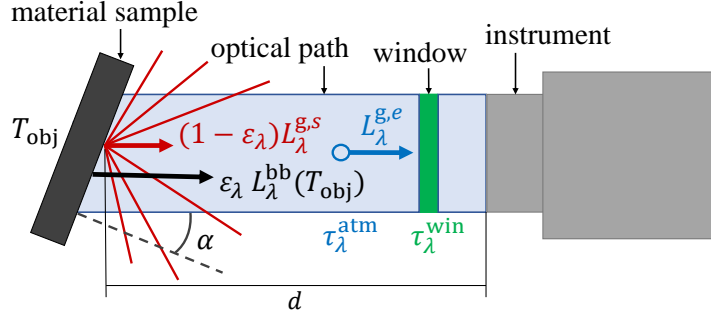


Figure 1: Schematic of the contributions to the radiance detected by the instrument. The collection volume is considered to be a cylinder of size $A \times d$, incident on the material surface with an angle α with respect to the surface normal.

where h is the Planck's constant, c is the speed of light and k_B is the Boltzmann's constant. Lastly, $L_\lambda^{g,e}$ is the spectral radiance emitted by the gas along the optical path, while $(1 - \varepsilon_\lambda)L_\lambda^{g,s}$ is the spectral radiance emitted by the surrounding gas and reflected by the material's surface onto the instrument collector optics.

In this work, we focus on the influence of $L_\lambda^{g,e}$ on the measured temperature; hence, the following assumptions are introduced. Considering highly emitting materials, i.e., $\varepsilon_\lambda \geq 0.8$, the contribution of $L_\lambda^{g,s}$ in the previous equation is considered negligible. However, we remark that this could become important in case of highly reflective surfaces. Moreover, for an instrument with operating range around $1 \mu\text{m}$ and a stand-off distance of 1m , we consider a thin optical path ($\tau_\lambda^{\text{atm}} \approx 1$). Finally, we also assume that the window material is carefully chosen to provide a uniform spectral transmittance in the instrument wavelength range, such that $\tau_\lambda^{\text{win}} = \tau_{\text{win}}$.

Inserting eq. 2 in eq. 1, and considering the aforementioned assumptions, the ratio, ρ_m , of the signals, S_1 and S_2 , output from each wavelength band of a two-color pyrometer writes

$$\rho_m = \frac{S_1}{S_2} \approx \frac{k_1}{k_2} \times \frac{\int_{\Delta\lambda_1} \tilde{R}_{\lambda,1} [\varepsilon_\lambda L_\lambda^{\text{bb}}(T_{\text{obj}}) + L_\lambda^{g,e}] d\lambda}{\int_{\Delta\lambda_2} \tilde{R}_{\lambda,2} [\varepsilon_\lambda L_\lambda^{\text{bb}}(T_{\text{obj}}) + L_\lambda^{g,e}] d\lambda}, \quad (4)$$

where the factor $\varphi = k_1/k_2$ accounts for the absolute sensitivity ratio between $R_{\lambda,1}$ and $R_{\lambda,2}$. Since only the normalized responses $\tilde{R}_{\lambda,i}$ are generally provided by the manufacturer, this coefficient can be determined during calibration, as later discussed in section 3.2. The previous equation also considers the same optical throughput for the two measuring bands, i.e., $\Theta_1 = \Theta_2$, which is the case for dual sandwich detectors considered in this work.

During calibration, performed in a controlled laboratory environment at room

temperature, optical path emission is negligible, i.e., $L_\lambda^{\text{g,e}} \approx 0$, and a blackbody calibration source provides $\varepsilon_\lambda \approx 1$. Hence, eq. 4 reduces to

$$\rho_c = \varphi \frac{\int_{\Delta\lambda_1} \tilde{R}_{\lambda,1} L_\lambda^{\text{bb}}(T_{\text{obj}}) d\lambda}{\int_{\Delta\lambda_2} \tilde{R}_{\lambda,2} L_\lambda^{\text{bb}}(T_{\text{obj}}) d\lambda} = \mathcal{H}_c(T_{\text{obj}}), \quad (5)$$

where ρ_c indicates the signal ratio obtained during calibration and \mathcal{H}_c represents the calibration curve. During measurements in a PWT, instead, emission from the high-temperature plasma along the optical path will affect the measured ratio when $L_\lambda^{\text{g,e}} \approx \varepsilon_\lambda L_\lambda^{\text{bb}}(T_{\text{obj}})$. In this case, as ρ_m will differ from ρ_c for the same value of T_{obj} , one only measures the apparent temperature

$$T_{\text{app}} = \mathcal{H}_c^{-1}(\rho_m), \quad (6)$$

and the quantity

$$e = \frac{T_{\text{app}} - T_{\text{obj}}}{T_{\text{obj}}} \times 100 \quad (7)$$

will describe the relative measurement error percent in the following analysis. Eq. 4, eq. 5 and eq. 6 represent the Instrument Response Model (IRM) that will be used to study the effect of the gas emission along the line of sight on the temperature measured by means of TCP. For this, we consider a target material with uniform spectral emittance in the instrument range, in order to satisfy the gray-body assumption of ratio pyrometry.

3. Experimental set-up and calibration

3.1. The VKI Plasmatron facility

The VKI Plasmatron facility, rendered in Figure 2(a), is equipped with a 160 mm diameter ICP torch, powered by a 400 kHz, 1.2 MW, 2 kV electric generator and connected to a 1.4 m diameter, 2.4 m long test chamber. An extensive description of the facility and its performance was given by Bottin and co-workers [44–46]. Fig. 2(b) shows a schematic section of the test chamber and ICP torch. The latter is made up of a quartz tube, surrounded by a six-turn flat coil inductor and supplied by a gas injection system. The electric power to the coil, P_{el} , is monitored by a voltage-current probe, while a calibrated flow meter (F-203AV, Bronkhorst High-Tech B.V, NL) controls the mass flow rate, \dot{m}_{gas} , of the test gas supplied to the torch. The gas, compressed atmospheric air in this case, is heated by electromagnetic induction, thus providing a chemically pure plasma flow. Pressure in the test chamber, p_c , is measured by an absolute pressure transducer (Membranovac DM 12, Leybold GmbH, DE). The material sample is mounted onto a movable probe holder, which can be injected into the plasma flow at a distance of 385 mm from the torch exit.

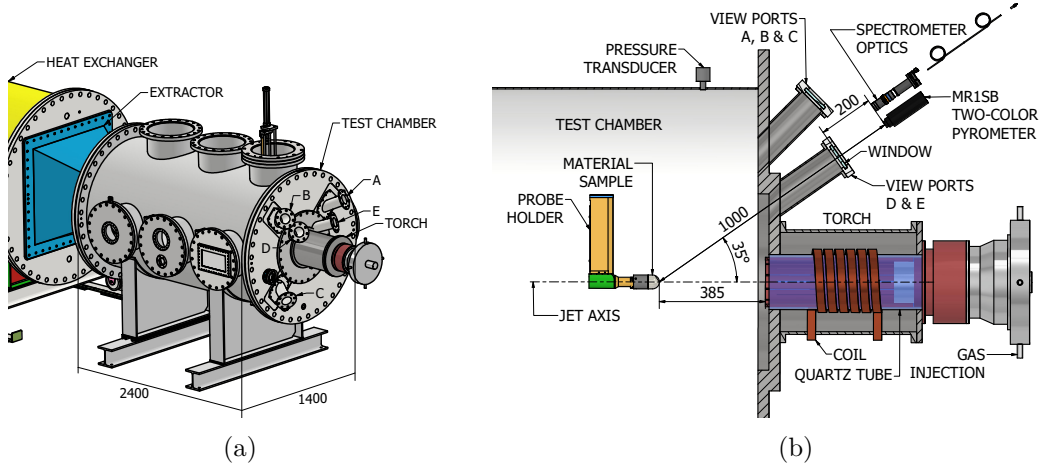


Figure 2: (a) Rendering of the VKI Plasmatron facility, showing the test-chamber and the location of the view ports. (b) Schematic of the experimental set-up, highlighting the main components of the ICP torch and the geometry of the optical paths of the two-color pyrometer and spectrometer. Dimensions in millimeters.

3.2. Two-color pyrometer and calibration

We used the Marathon Series MR1SB (Raytek Corporation, USA) two-color pyrometer, featuring a sandwich silicon detector with spectral responsivities between 0.75-1.15 μm and 0.95-1.15 μm (Fig. 3(a)) and a temperature range between 973 K and 2073 K. Signals were recorded with an integration time of 10 ms and at a frequency of 10 Hz. Optical access to the Plasmatron test chamber was provided through a 1.5 cm thick quartz window (label D in Fig. 2(a)), whose spectral transmission in the instrument range can be considered uniform with a value $\tau_{\text{win}} \approx 0.87$. The instrument is placed at 1 m distance from the sample and the optical access provides an inclination of about 35° with respect to the surface normal. The probing area over the sample surface has a size of approximately 14 mm in diameter.

The radiometric calibration of the instrument was performed with a variable temperature blackbody source (R1500T, Ametek Landcal, UK) in the range 973-1773 K. The latter features a 120° conical-ended silicon-carbide cavity with a 40 mm clear aperture and a PID controller to hold the set temperature. The uncertainty on the source temperature is ± 3 K, while its emittance is considered unitary and spectrally uniform in the instrument wavelength range (0.75-1.15 μm).

During calibration, the two-color pyrometer is placed in front of the calibration source, replicating the operating distance and position of the window along the optical path. Then, the signal output from each band is recorded for a set of source temperatures to provide the calibration points. Figure 3(b) shows the

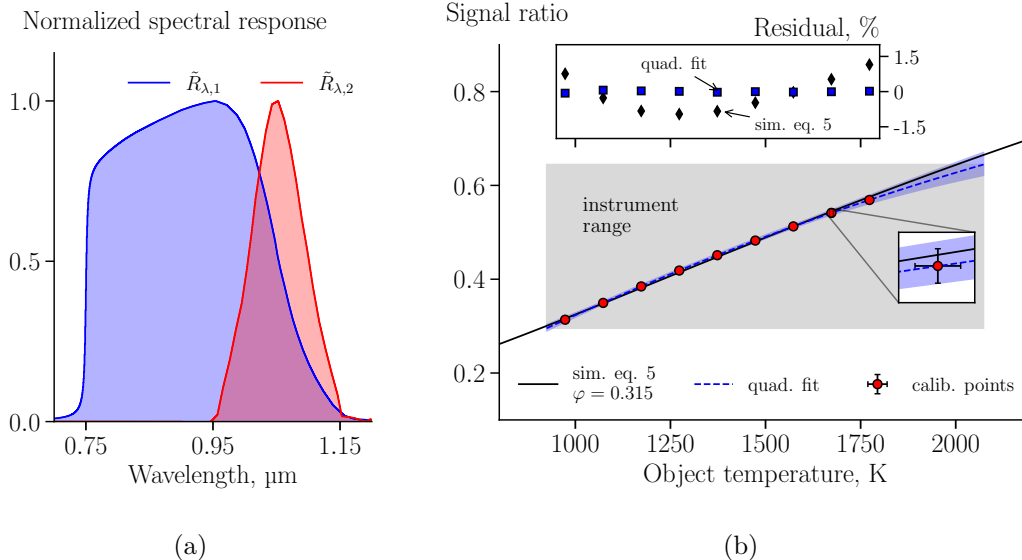


Figure 3: (a) Normalized spectral responses, $\tilde{R}_{\lambda,1}$ and $\tilde{R}_{\lambda,2}$, of the Raytek Marathon Series MR1SB two-color pyrometer. (b) Simulated signal ratio from eq. 5 closely matches the calibration points to a maximum residual of 1.5%, after fitting the modulation factor ($\varphi = 0.315$). A quadratic function fits the calibration points with negligible residuals and will be used to process the actual experimental data in sec. 5.

signal ratio, ρ_c , as a function of T_{obj} . A value of $\varphi = 0.315$ allowed to best fit the simulated response through eq. 5 to the calibration points, with a residual within $\pm 1.5\%$. This deviation, although very limited, can be related to an imperfect knowledge of the sensor responsivities. While the simulated response will be used in sec. 4 to study the effect of $L_{\lambda}^{\text{g},e}$ on the measured temperature, a quadratic function fits the calibration points with negligible residuals and will be used in sec. 5 to process the actual experimental data. The quadratic fit is extrapolated to 2073 K to cover the whole instrument range. Uncertainties are propagated through the processing steps with a Monte Carlo sampling approach. We consider $\pm 3\text{K}$ on the calibration source temperature and $\pm 1\%$ on both S_1 and S_2 , including resolution and repeatability. This leads to about $\pm 1.5\%$ uncertainty on the measured temperature, excluding possible biasing effects.

3.3. Spectrometer and calibration

We used a compact spectrometer (MAYA 2000 PRO series, Ocean Insight, USA), coupled to a custom collection optics, as shown in Fig. 4(a), to probe the spectral radiance emitted by the surface of the material sample within the 750 – 1030 nm range. The spectrometer features a 25 μm wide entrance slit, a 300 grooves/mm grating and a back-thinned 2D CCD detector. The integration

time was set to 1 s and the instrument was triggered at a frequency of 0.5 Hz by a pulse generator (DG535, Stanford Research Systems, USA), allowing precise synchronization with the two-color pyrometer.

The collection optics consists of a 550 μm core diameter multi-mode optics fiber, a 75 mm focal length achromatic lens, a 455 nm high-pass filter and a 5 mm diameter iris. The optics are mounted on a 1 inch diameter tube, held by a kinematic mount for precise alignment to the material surface. A stack of Neutral Density (ND) filters is additionally mounted to decrease the detected irradiance and avoid saturation of the detector. Optical access to the Plasmatron chamber was provided through a 5 mm thick CaF_2 window (label E in Fig. 2(a)), offering $\sim 95\%$ transmission in the wavelength range. In a similar configuration to the two-color pyrometer, the collection optics are placed at ~ 100 cm from the sample surface with a $\sim 35^\circ$ inclination with respect to its normal. The probing area has a size of about 10 mm in diameter on the sample surface. The spectral resolution was characterized with a low-pressure Ar lamp, resulting in about 0.75 μm full-width at half maximum.

The system was calibrated using the same reference blackbody source described previously, for a source temperature of 1773 K and reproducing the optical path encountered in the measurement. Indicating with $\hat{U}_\lambda = U_\lambda - U_{\lambda,\text{bg}}$ the raw signal detected by the spectrometer, U_λ , minus the background signal, $U_{\lambda,\text{bg}}$, (in digital intensity counts) and with Δt the integration time, the measured spectral radiance L_λ^{m} is obtained as [47]

$$L_\lambda^{\text{m}} = \frac{\hat{U}_\lambda^{\text{m}}}{\Delta t_{\text{m}}} \cdot f_\lambda^{\text{c}}, \quad (8)$$

where

$$f_\lambda^{\text{c}} = \frac{L_\lambda^{\text{bb}}}{\hat{U}_\lambda^{\text{c}}/\Delta t_{\text{c}}} \quad [\text{mW ms}/(\text{count cm}^2 \mu\text{m sr})] \quad (9)$$

is the calibration factor and the letters "m" and "c" indicate the quantities recorded during measurement and calibration, respectively. Figure 4(b) shows the calibration factor as a function of wavelength. The calibration law assumes linearity of the signal \hat{U}_λ with respect either to the incident radiance and integration time, which was checked during calibration.

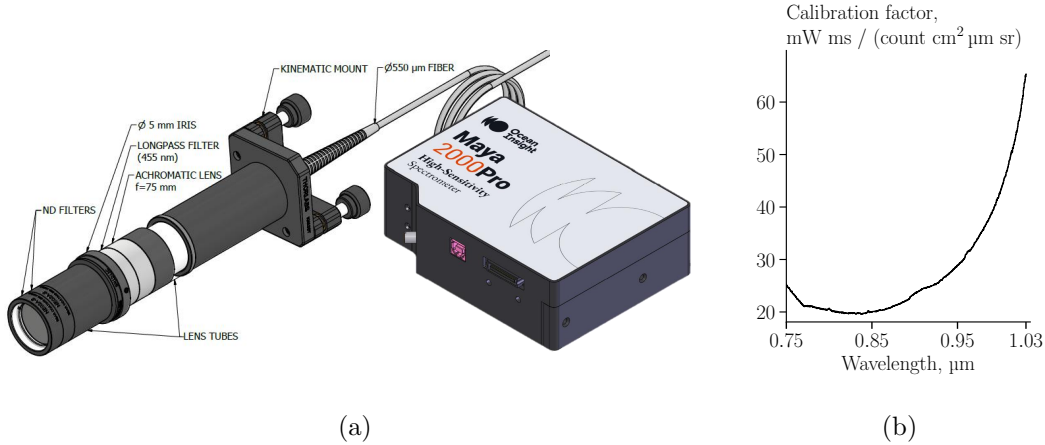


Figure 4: (a) Rendering of the compact spectrometer, together with the optical set-up designed for this work. (b) Calibration factor of the spectrometer as a function of wavelength.

4. Numerical assessment of the measurement error due to plasma emission along the line of sight

4.1. Plasma flow field

The subsonic plasma flow in the Plasmatron chamber was numerically simulated using a two-dimensional magnetohydrodynamic solver, referred to as CF-ICP in the following, which couples the Maxwell induction equations with the Navier-Stokes equations under the assumptions of Local Thermodynamic Equilibrium (LTE) and axisymmetric steady flow [48]. The code is integrated into the Computational Object-Oriented Library for Fluid Dynamics (COOLFluid) [49] and relies on the Mutation++ library [50] to compute the thermodynamic and transport properties of an eleven-species air mixture (O_2 , N_2 , O_2^+ , N_2^+ , NO , NO^+ , O , O^+ , N , N^+ , e^-). Under well-established assumptions, the flow in the ICP torch can be considered continuum, partially ionized, and collision-dominated [51]. Then, the Navier-Stokes equations are used to express mass, momentum and energy conservation. The electromagnetic field is modeled with a simplified form of Maxwell's induction equation, coupled with the momentum and energy equations through Lorentz force and Joule heating effects. As the Reynolds number is typically low ($Re \sim 100$), the flow is assumed to be laminar and transition is neglected. The LTE model is adopted, where energy modes are assumed to follow a Maxwell-Boltzmann distribution and equilibrium chemistry occurs.

Figure 5(a) shows an example of the simulated temperature field. The domain includes the torch and a portion of the test chamber up to 500 mm from the torch exit and 160 mm from the jet axis, as well as a representative 50 mm diameter hemispherical probe positioned at 385 mm downstream of the torch. A

quadrilateral mesh with 16 000 cells was used for the computation and a convergence study confirmed the grid independence. Boundary conditions are specified in terms of the torch and probe wall temperature ($T_w = 350$ K), chamber pressure ($p_c = 50$ mbar), inlet gas mass flow rate ($\dot{m}_{\text{gas}} = 16$ g/s) and input numerical electric power ($P_{\text{el}}^{\text{sim}}$). Nine simulations were carried out for $50 \text{ kW} < P_{\text{el}}^{\text{sim}} < 130 \text{ kW}$, with increasing steps of 10 kW. In this regard, it is important to notice that $P_{\text{el}}^{\text{sim}}$ differs from the value measured experimentally, P_{el} , due to the energy efficiency of the ICP torch. Recent comparison with spectroscopic temperature measurements of the gas at different axial locations suggested that $P_{\text{el}}^{\text{sim}}/P_{\text{el}} \cong 35\text{-}40\%$ [33].

The figure also represents a 1 m long optical slab (ζ -axis), originating from the surface of the probe with a 35° inclination with respect to the jet axis and reaching the two-color pyrometer. Figure 5(b) shows the gas temperature and pressure along the optical slab for the different values of $P_{\text{el}}^{\text{sim}}$. Temperature increases rapidly through the boundary layer around the probe, up to several thousands of Kelvin, and drops to 350 K outside the jet core, i.e., for $\zeta > 150$ mm. Pressure, instead, is fairly uniform in the test chamber.

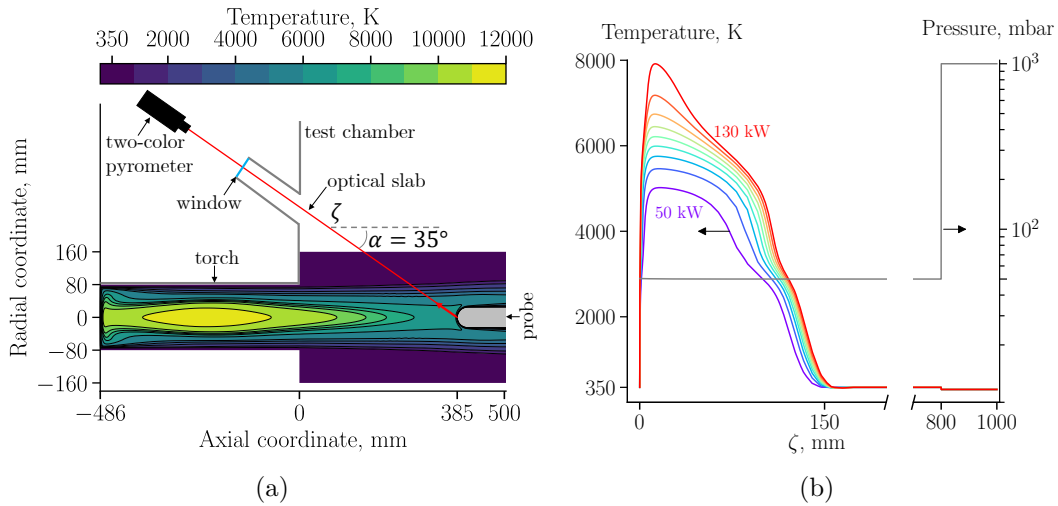


Figure 5: (a) Temperature field of the VKI Plasmatron ICP torch, simulated with CF-ICP code for an eleven-species air mixture with $p_c = 50$ mbar, $\dot{m}_{\text{gas}} = 16 \text{ g s}^{-1}$ and $P_{\text{el}}^{\text{sim}} = 90 \text{ kW}$. Also represented is the 1 m optical slab from the material sample to the instrument collection optics. (b) Temperature and pressure distributions along the optical slab, extracted from the CFD simulations as a function of $P_{\text{el}}^{\text{sim}}$. Since the domain is limited to 160 mm from the jet axis, values are extrapolated up to the position of the window ($\zeta = 800$ mm), while laboratory conditions ($T = 300$ K and $p = 1$ atm) are considered for $800 \text{ mm} < \zeta < 1000$ mm.

Since the simulation domain terminates at 160 mm from the jet axis, corresponding to 278 mm along ζ , quantities were uniformly extrapolated up to the position of the window, i.e., $\zeta = 800$ mm, while outside the test chamber, i.e., for $\zeta > 800$ mm, we assume laboratory conditions with $T = 300$ K and $p = 1$ atm.

In order to reduce the computational effort related to the CFD simulations, the temperature on the surface of the probe was fixed at 350 K. During a PWT experiment, instead, this will rise to an equilibrium value as a result of the heat transfer between the gas and the material. As the thermal boundary layer around the probe is very small (~ 5 mm) with respect to the jet core (~ 150 mm), where much of the emission is originating, we expect a limited effect on $L_\lambda^{\text{g,e}}$.

While a detailed validation of the CFD simulations of the plasma flow field is currently missing, the following analysis aims to show the principal effects of plasma emission on the measured surface temperature, providing better understanding and interpretation of the experimental results.

4.2. Line-of-sight and surface radiance

We used the Non-Equilibrium Air Radiation (NEQAIR v.15.0) code [52, 53] to simulate the spectral radiance emitted by the plasma along the line of sight. This allows to compute line-by-line radiation spectra, including spontaneous emission, absorption and stimulated emission, due to transitions between different energy states of atomic and molecular species through a non-uniform gas mixture. Inputs to the code are the gas temperature and number density of constituent species along the optical path, which were provided by the aforementioned CFD simulations. Considering LTE, the population of the excited states is assumed to follow a Boltzmann distribution.

For different values of $P_{\text{el}}^{\text{sim}}$, Fig. 6 shows the simulated $L_\lambda^{\text{g,e}}$ spectra in the 0.7-1.2 μm range. For visualization purposes, the spectral resolution was downgraded through a convolution with a Gaussian lineshape of 0.75 nm at full-width at half maximum. The lines originating from excited states of O and N atoms are clearly evident, together with the background radiation, mainly due to the first-positive rovibronic transition of N_2 . In the same plot, the spectral radiance $L_\lambda^{\text{obj}} = \varepsilon_\lambda L_\lambda^{\text{bb}}(T_{\text{obj}})$, from a gray-body with $\varepsilon_\lambda = 0.85$, is also shown for different values of the object temperature between 750 K and 2000 K.

Lastly, the shaded gray areas represent the sensitive wavelength bands of the MR1SB two-color pyrometer. We can observe how emission from the plasma easily overcomes the object's radiance up to $T_{\text{obj}} = 1000$ K, while the peaks corresponding to the atomic lines achieve comparable values even above $T_{\text{obj}} = 1500$ K. Additionally, since $L_\lambda^{\text{g,e}}$ is highly non-uniform within the sensitive bands of the two-color pyrometer, the ratio of the detected signals can be strongly affected.

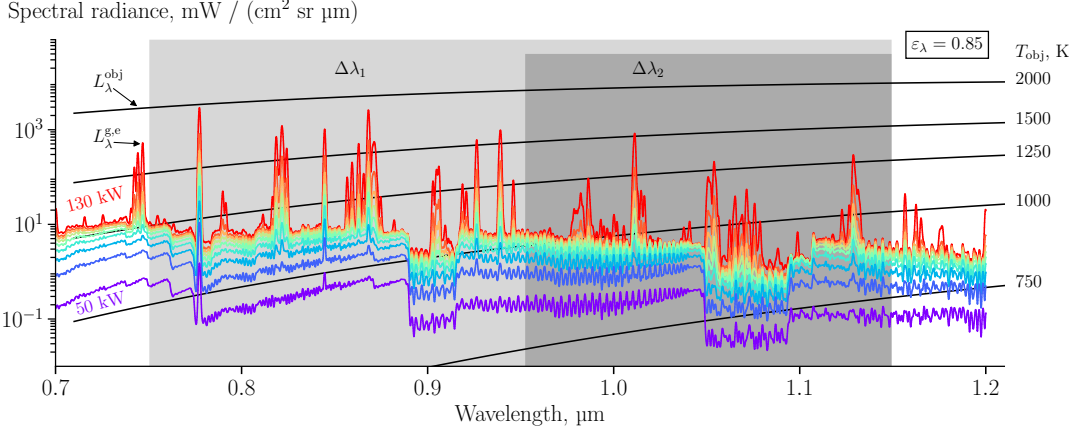


Figure 6: Comparison between the simulated values of $L_{\lambda}^{g,e}$ and $L_{\lambda}^{obj} = \varepsilon_{\lambda} L_{\lambda}^{bb}(T_{obj})$, for different values of T_{obj} and $\varepsilon_{\lambda} = 0.85$. The emission originating from the plasma along the instrument optical path can significantly interfere with the object's emission up to 1500 K.

4.3. Sample visibility factors

For a range of temperatures $500 \text{ K} < T_{obj} < 2000 \text{ K}$ and $\varepsilon_{\lambda} = 0.85$, we compute the sample band visibility factors, $\nu_{\Delta\lambda_i}$, adapting the definition of Sakuta and Boulos [37] to consider also the instrument spectral response in each band

$$\nu_{\Delta\lambda_i} = \frac{\int_{\Delta\lambda_i} \tilde{R}_{\lambda,i} \varepsilon_{\lambda} L_{\lambda}^{bb}(T_{obj})}{\int_{\Delta\lambda_i} \tilde{R}_{\lambda,i} [\varepsilon_{\lambda} L_{\lambda}^{bb}(T_{obj}) + L_{\lambda}^{g,e}]}. \quad (10)$$

These coefficients relate the detected object emission to the sum of the object and plasma emission along the line of sight, clearly showing the plasma interference effect on radiation thermometry.

In Fig. 7(a) we can appreciate the trend of $\nu_{\Delta\lambda_1}$ and $\nu_{\Delta\lambda_2}$ with T_{obj} for different values of P_{el}^{sim} . Both visibility factors are close to zero until 750 K, below which the plasma emission overcomes significantly the object emission and prevents its detection. A transition region is observed for $750 \text{ K} < T_{obj} < 1500 \text{ K}$, where object and plasma emission have similar intensities. Only above 1500 K the plasma emission becomes negligible and the visibility factors approach one. Additionally, Fig. 7(b) shows the value of T_{obj} as a function of P_{el}^{sim} for which $\nu_{\Delta\lambda_i} = 0.99$ and $\nu_{\Delta\lambda_i} = 0.90$, respectively. This highlights that, for a certain value of the object temperature, the visibility factors have different values in each band, which can further increase the biasing effect on the measured signal ratio.

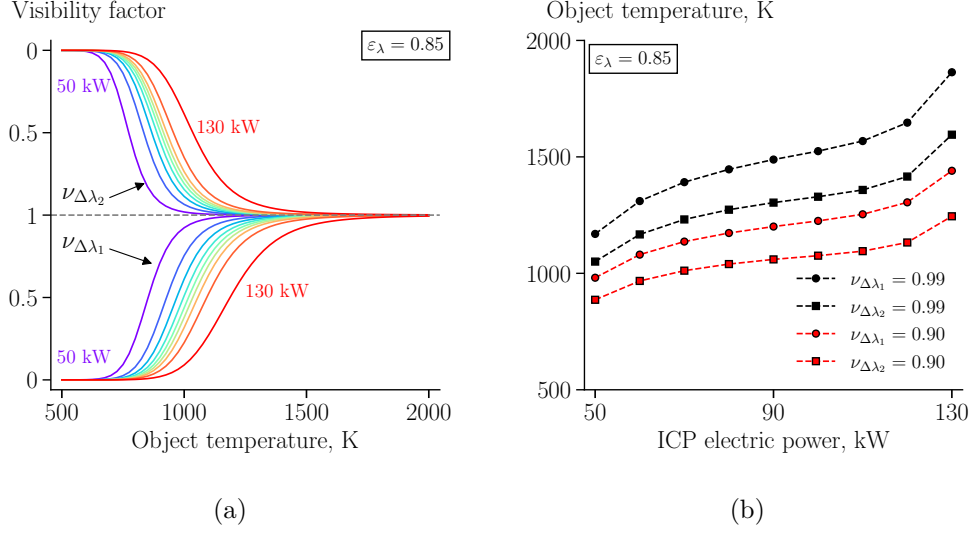


Figure 7: (a) Sample visibility factors, $\nu_{\Delta\lambda_1}$ and $\nu_{\Delta\lambda_2}$, as a function of the object temperature, for different values of $P_{\text{el}}^{\text{sim}}$ and for $\varepsilon_\lambda = 0.85$. (c) Object temperature for which $\nu_{\Delta\lambda_i} = 0.99$ and $\nu_{\Delta\lambda_i} = 0.90$, as a function of $P_{\text{el}}^{\text{sim}}$, for $\varepsilon_\lambda = 0.85$.

4.4. Simulated apparent temperature and measurement error

Using the instrument response model formulated in sec. 2, we simulate the effect of the plasma emission on the measured apparent temperature. For $\varepsilon_\lambda = 0.85$ and $500 \text{ K} < T_{\text{obj}} < 2500 \text{ K}$, $L_\lambda^{\text{g},e}$ is inserted in eq. 4 to simulate the measured signal ratio. Then, the apparent temperature is computed from eq. 6. Depending on the value of $P_{\text{el}}^{\text{sim}}$, Fig. 8(a) clearly demonstrates that T_{app} deviates considerably from T_{obj} when the latter is below 1500 K. Correspondingly, the relative error is computed according to eq. 7 and shown in Fig. 8(b). A large systematic error is found for low values of T_{obj} , while the steepness of the curves demonstrates the high sensitivity to $L_\lambda^{\text{g},e}$.

Figure 8(c) synthetically depicts a map of the error induced by $L_\lambda^{\text{g},e}$, where each curve represents $e = 1\%$ as a function of T_{obj} and ε_λ . A large portion of the instrument range can be affected by errors larger than 1%, this being more pronounced for high values of $P_{\text{el}}^{\text{sim}}$ and low values of ε_λ . However, we should notice that an instrument with a higher temperature range is typically selected for high values of $P_{\text{el}}^{\text{sim}}$ to accommodate the higher values also expected for T_{obj} . Moreover, a horizontal asymptote is reached for $\varepsilon_\lambda \rightarrow 0$, since the instrument would only detect the plasma radiation in this limit condition. This graph is useful to provide a first estimation of the error induced by $L_\lambda^{\text{g},e}$ on the measured temperature, knowing approximately the expected values of T_{obj} and ε_λ for a selected power condition during the experiment.

4.5. Simulated effect during transient heating

Finally, we analyze the effect occurring during the transient heating phase of a material sample for a PWT experiment. As the latter is injected into the plasma flow, we consider the time evolution of the surface temperature to follow the analytical function

$$T_{\text{obj}}(t) = \begin{cases} T_0 & \text{for } t < 0 \text{ s} \\ T_0 + g [1 - (1 + \omega_0 t) \exp(-\omega_0 t)] & \text{for } t > 0 \text{ s,} \end{cases} \quad (11)$$

which represents the step response of a critically damped second order system, with gain g and natural frequency ω_0 . We assume an initial temperature of $T_0 = 350 \text{ K}$, while $g = 1250 \text{ K}$ and $\omega_0 = 0.1 \text{ s}^{-1}$ provide a steady-state temperature of 1600 K after 80 s . These values are selected to represent qualitatively the experimental results, discussed later in sec. 5. Figure 8(d) shows $T_{\text{obj}}(t)$, along with the simulated behavior of the apparent temperature, $T_{\text{app}}(t)$, as it would be measured by the two-color pyrometer including the effect of $L_{\lambda}^{\text{g,e}}$ for two representative conditions with $P_{\text{el}}^{\text{sim}} = 60 \text{ kW}$ and $P_{\text{el}}^{\text{sim}} = 80 \text{ kW}$, considering $\varepsilon_{\lambda} = 0.85$. The bias induced by the gas radiation along the instrument line of sight causes T_{app} to drop from large values, rather than to follow the rising trend of T_{obj} , thus resulting in a significant error during the transient heating. As time evolves, the apparent temperature approaches the object temperature when this becomes high enough for $L_{\lambda}^{\text{g,e}}$ to become negligible.

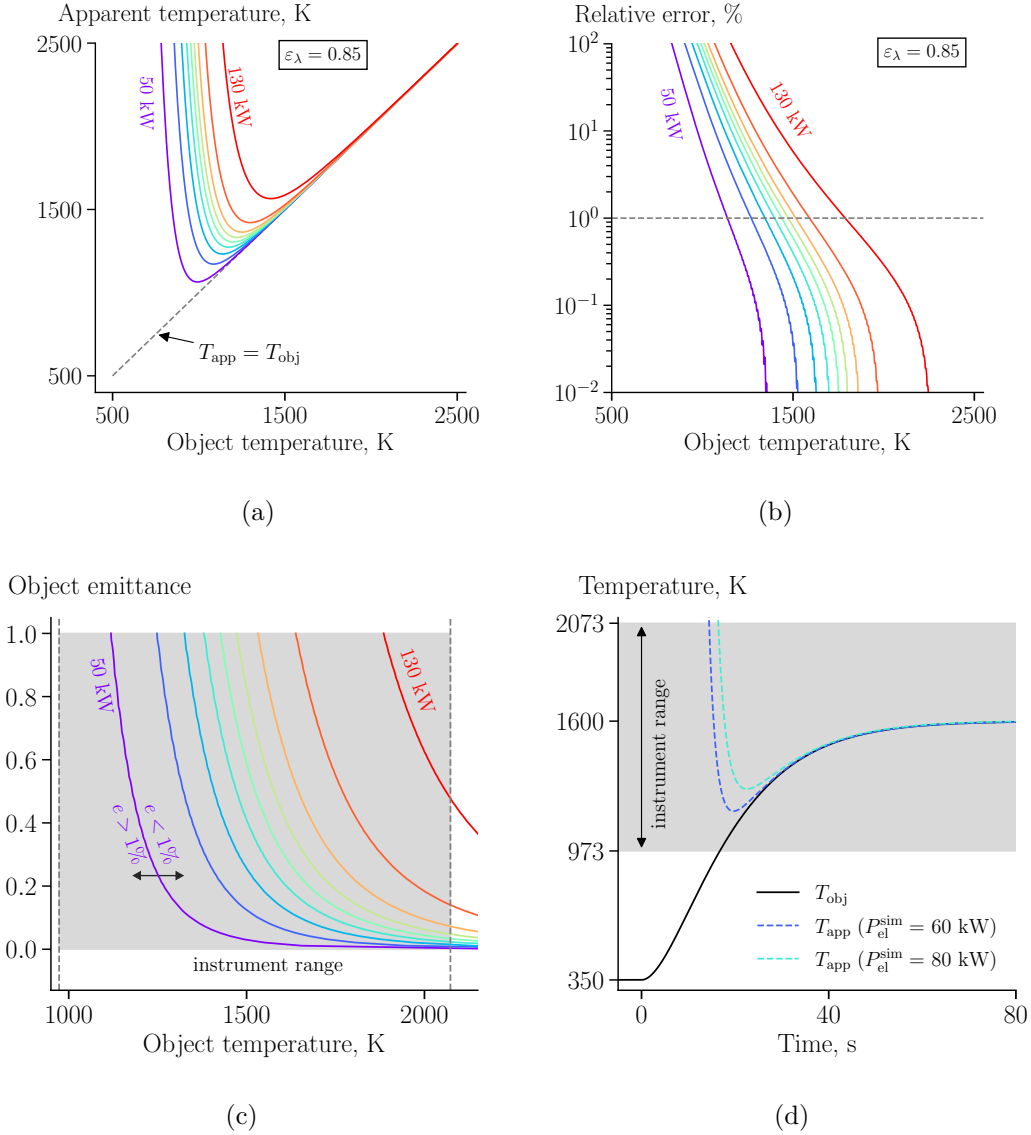


Figure 8: (a) Simulated effect of $L_\lambda^{g,e}$ on T_{app} for $\varepsilon_\lambda = 0.85$, as a function of P_{el}^{sim} . (b) Relative error percent of T_{app} with respect to T_{obj} for $\varepsilon_\lambda = 0.85$, as a function of P_{el}^{sim} . (c) Map of the simulated measurement error induced by $L_\lambda^{g,e}$ as a function of T_{obj} and ε_λ . Each line represents $e = 1\%$ and separates the regions for which $e > 1\%$ and $e < 1\%$, respectively. (d) Expected material temperature during a PWT experiment, T_{obj} , and correspondent simulated apparent temperature, T_{app} , as it would be measured by the two-color pyrometer considering the influence of $L_\lambda^{g,e}$ for $P_{el}^{sim} = 60$ kW and $P_{el}^{sim} = 80$ kW. A positive bias induces T_{app} to decrease during the transient heating and to approach T_{obj} only when its value is high enough.

5. Experimental results and discussion

5.1. Material sample and test conditions

Figure 9(a) shows the ceramic matrix composite sample (Keraman C/SiC, MT-Aerospace) that was selected to study the effect of $L_\lambda^{\text{g,e}}$ on TCP during a PWT experiment. The material is a 26.5 mm diameter, 3 mm thick disc, made up of a carbon fiber matrix, with 7 μm diameter filaments, and treated with a polymer vapor infiltration before a final coating (60-80 μm thick) with SiC by chemical vapor deposition. Room temperature spectral reflectance, r_λ , was characterized before the experiment using a Cary-500 spectrophotometer (Agilent Technologies Inc., USA). The normal spectral emittance in Fig. 9(b), obtained as $\varepsilon_\lambda = 1 - r_\lambda$, shows a uniform value within 0.75-1.15 μm , close to 0.85. Hence, this allowed to rely on the gray-body assumption for TCP within the instrument range, as well as to consider a negligible influence of $L_\lambda^{\text{g,s}}$ due to the large value of ε_λ . Figure 9(c) shows a picture during the plasma exposure, where the material sample was mounted on the 50 mm diameter ESA standard probe and positioned at 385 mm from the ICP torch exit. The experimental values, defining the test conditions achieved in the VKI Plasmatron facility, are reported in table 1.

Table 1: Plasmatron experimental conditions, listing the distance to the torch exit, duration of the plasma exposure, electric power P_{el} , test gas mass flow rate \dot{m}_{gas} and chamber pressure p_c .

distance mm	duration s	gas	P_{el} kW	\dot{m}_{gas} g/s	p_c mbar
385 ± 1	300	air	160 ± 10	16 ± 0.15	50 ± 1

5.2. Two-color pyrometry measurement and correction

The time evolution of the measured signals from the two wavelength bands, S_1 and S_2 , is shown in Fig. 10(a). Here, $t = 0$ s represents the instant when the sample is injected into the plasma flow. After a transient heating phase of approximately 80 s, the signals settle to a steady value; then, the plasma torch is switched off at $t = 300$ s, allowing to record the sample cool down until $t = 400$ s.

We can notice that both S_1 and S_2 drop at $t = 0$ s, as the sample obstructs the lower half of the plasma jet after injection. Moreover, shortly after $t = 0$ s we can consider T_{obj} to be low enough such that $L_\lambda^{\text{g,e}} \gg L_\lambda^{\text{obj}}$ and $L_\lambda \approx L_\lambda^{\text{g,e}}$. We indicate with S_1^{ref} and S_2^{ref} the time-averaged signals within a reference interval Δt_{ref} shortly after the injection time, in this case between 0 s and 6 s. This range should be chosen according to the particular measurement condition and must end before the signals start to rise due to the emission from the object's surface. Since $L_\lambda \approx L_\lambda^{\text{g,e}}$ within Δt_{ref} , then eq. 1 yields

$$S_i^{\text{ref}} \approx k_i \Theta \int_{\Delta \lambda_i} \tilde{R}_{\lambda,i} L_\lambda^{\text{g,e}} d\lambda. \quad (12)$$

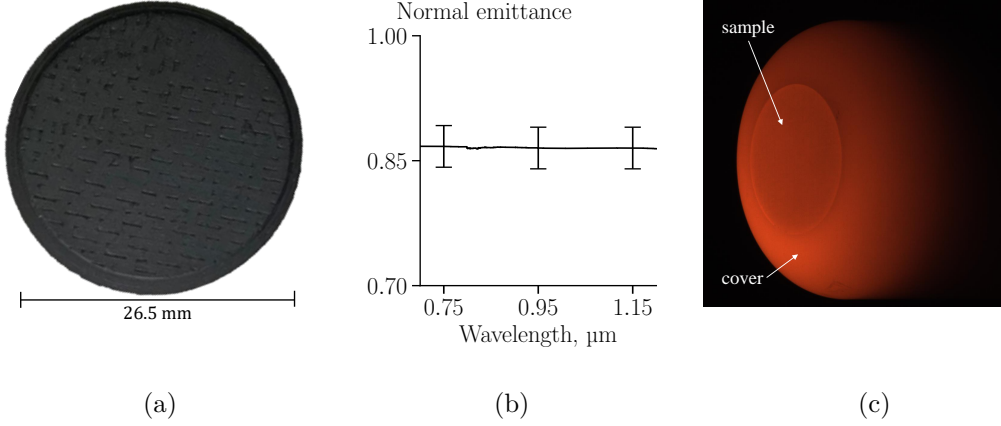


Figure 9: (a) Picture of the C/SiC sample before the experiment. (b) Normal spectral emittance obtained from room temperature reflectometry of the virgin sample shows $\varepsilon_\lambda \approx 0.85$, with a uniform behavior within 0.75-1.15 μm . (c) Picture taken during the plasma exposure, showing the material sample inserted into the probe cover.

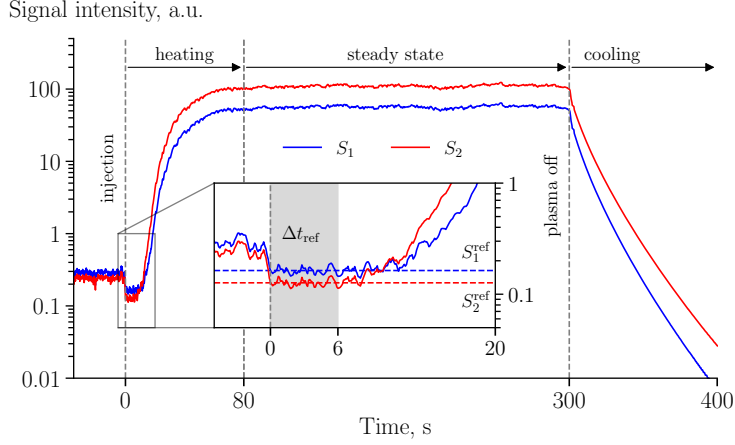
Assuming that $L_\lambda^{g,e}$ does not vary significantly during the sample heating and steady-state phases, the corrected signals

$$S_i^{\text{corr}} = \begin{cases} S_i - S_i^{\text{ref}} \approx k_i \Theta \int_{\Delta\lambda_i} \tilde{R}_{\lambda,i} \varepsilon_\lambda L_\lambda^{\text{bb}}(T_{\text{obj}}) d\lambda & \text{for } 0 \leq t \leq 300 \text{ s} \\ S_i & \text{for } t > 300 \text{ s} \end{cases} \quad (13)$$

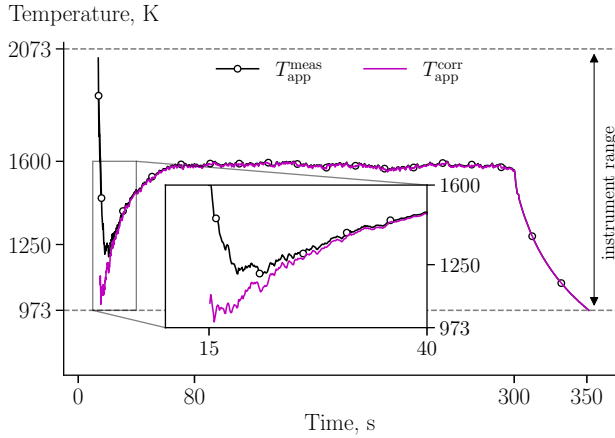
approximate the contributions originating from the object's surface only. Notice that a correction is not necessary after 300 s, as $L_\lambda^{g,e} = 0$ after the plasma is switched off.

The measured apparent temperature, $T_{\text{app}}^{\text{meas}}$, is obtained considering the ratio $\rho_m = S_1/S_2$ and applying the calibration curve obtained in sec. 3.2 as $T_{\text{app}} = \mathcal{H}_c^{-1}(\rho_m)$. The corrected ratio $\rho_m^{\text{corr}} = S_1^{\text{corr}}/S_2^{\text{corr}}$, instead, can be used to determine a corrected value of the apparent temperature $T_{\text{app}}^{\text{corr}} = \mathcal{H}_c^{-1}(\rho_m^{\text{corr}})$. The latter represents the best estimate of the object temperature, removing the biasing effect of the plasma emission along the line-of-sight. Figure 10(b) shows the measured and corrected temperature values. We can notice how, before correction, $T_{\text{app}}^{\text{meas}}$ follows a similar trend to those predicted by our simulations in Fig 8(d). Namely, the value drops from the top of the instrument range, to rise again only after $t \approx 20$ s. Hence, this peculiar trend can be associated to the biasing effect of $L_\lambda^{g,e}$ on the measured signal. The corrected temperature, instead, recovers a rising trend, as it is expected during the transient heating of the material. At steady state, the surface temperature is high enough for $L_\lambda^{g,e}$ to have a small effect and the correction has a negligible impact.

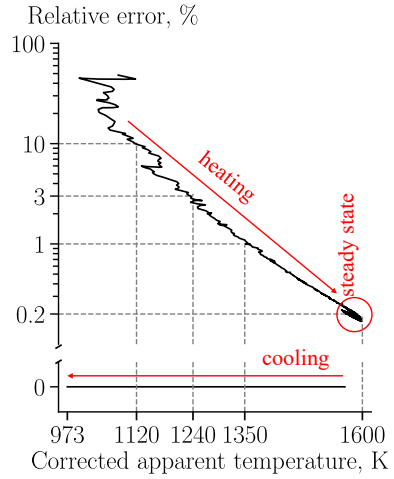
Considering $T_{\text{app}}^{\text{corr}}$ to be best representative of the material surface temperature,



(a)



(b)



(c)

Figure 10: (a) Measured signals S_1 and S_2 , showing the heating, steady-state and cooling phases. The reference signals for correction, S_1^{ref} and S_2^{ref} , are obtained by averaging the values within $0\text{ s} < t < 6\text{ s}$. (b) Comparison between the measured apparent temperature and its corrected value. Notice how $T_{\text{app}}^{\text{meas}}$ decreases during the heating phase, similarly to what has been shown in our simulations (Fig. 8(d)). $T_{\text{app}}^{\text{corr}}$, instead, recovers an increasing trend, as expected. (c) Relative error between the measured and corrected apparent temperature. $T_{\text{app}}^{\text{meas}}$ falls within 1% of $T_{\text{app}}^{\text{corr}}$ only above 1350 K, while their difference is negligible at steady state. Since no correction is applied during the cooling phase, their values coincide.

then $e = (T_{\text{app}}^{\text{meas}} - T_{\text{app}}^{\text{corr}})/T_{\text{app}}^{\text{corr}}$ represents the relative error of the measured value with respect to the corrected one. Figure 10(c) shows that $T_{\text{app}}^{\text{meas}}$ falls within 1% of $T_{\text{app}}^{\text{corr}}$ only above 1350 K, while the error is larger than 10% below 1120 K. Their

difference becomes negligible (0.2%) at steady state and, since no correction is applied after the plasma is switched off, their values coincide during the cooling phase.

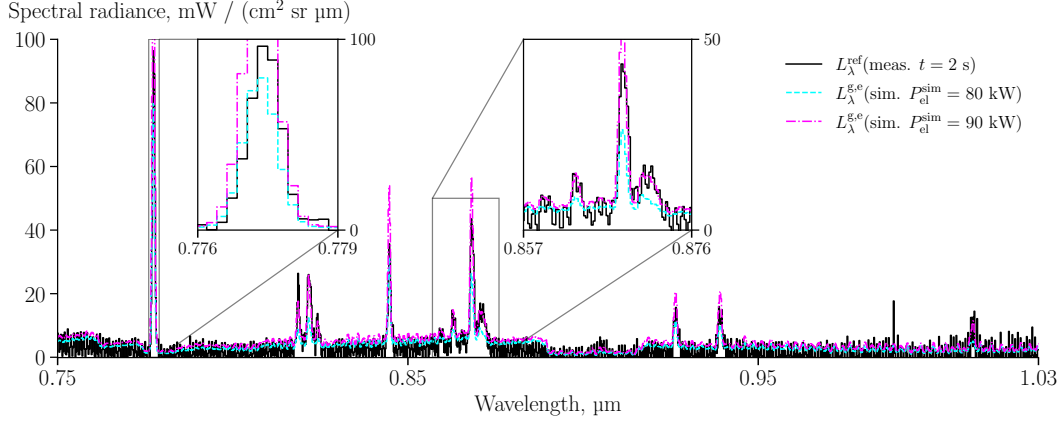
5.3. Comparison to spectrometry

The spectrometer, described in sec. 3.3, allowed to probe the spectral radiance emitted by the object's surface and gas along the line of sight. Following the previous discussion, since we expect $L_\lambda^{\text{obj}} \ll L_\lambda^{\text{g,e}}$ for $0 \text{ s} < t < 6 \text{ s}$, a reference spectrum L_λ^{ref} within this time interval is such that $L_\lambda^{\text{ref}} \cong L_\lambda^{\text{g,e}}$. Figure 11(a) compares L_λ^{ref} at $t = 2 \text{ s}$ to the values of $L_\lambda^{\text{g,e}}$, computed in sec. 4.2 for $P_{\text{el}}^{\text{sim}} = 80 \text{ kW}$ and $P_{\text{el}}^{\text{sim}} = 90 \text{ kW}$, demonstrating that our radiative transfer simulations provide comparable intensities to those observed during actual experiments.

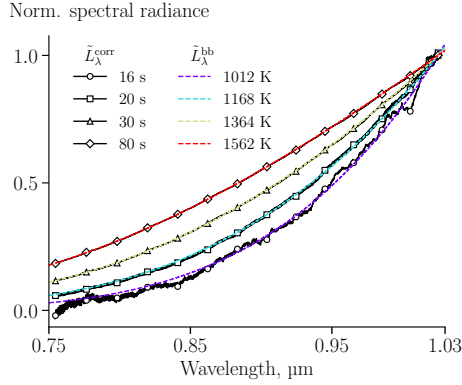
To measure the surface temperature from the observed spectra, these are first corrected for the reference spectrum as

$$\begin{cases} L_\lambda^{\text{corr}} = L_\lambda^{\text{m}} - L_\lambda^{\text{ref}} \cong \varepsilon_\lambda L_\lambda^{\text{bb}}(T_{\text{obj}}) & \text{for } 0 \leq t \leq 300 \text{ s} \\ L_\lambda^{\text{corr}} = L_\lambda^{\text{m}} & \text{for } t > 300 \text{ s.} \end{cases} \quad (14)$$

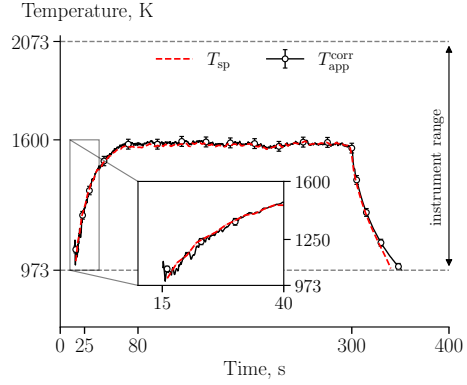
Then, employing a similar method to the one shown by Savino et al. [20], the material's surface temperature can be obtained by a least-square fitting of the normalized spectrum $\tilde{L}_\lambda^{\text{corr}} = L_\lambda^{\text{corr}}/L_{\lambda_{\text{norm}}}^{\text{corr}}$ with the normalized Planck distribution $\tilde{L}_\lambda^{\text{bb}}(T) = L_\lambda^{\text{bb}}(T)/L_{\lambda_{\text{norm}}}^{\text{bb}}(T)$. For this procedure we consider $\lambda_{\text{norm}} = 1.03 \mu\text{m}$, while the fitting provides the temperature T_{sp} . Figure 11(b) shows some representative $\tilde{L}_\lambda^{\text{corr}}$ spectra at different times, together with the fitted $\tilde{L}_\lambda^{\text{bb}}(T_{\text{sp}})$ spectra, and the corresponding temperatures. Before $t = 16 \text{ s}$, however, the signal is too low to provide reliable measurements. Figure 11(c) compares the measured surface temperature by means of the spectroscopic method, T_{sp} , together with the corrected value from the two-color ratio pyrometry, $T_{\text{app}}^{\text{corr}}$, obtained in the previous section. Their values show a close agreement, confirming that the subtraction of the reference signals correspondent to the line-of-sight plasma radiation allows to recover a reliable measurement of the material surface temperature during the transient heating phase.



(a)



(b)



(c)

Figure 11: (a) Reference spectrum, L_{λ}^{ref} , measured at $t = 2$ s, representing the spectral radiance of the gas along the optical path. Simulated $L_{\lambda}^{\text{g,e}}$ spectra for $P_{\text{el}}^{\text{sim}} = 80$ and 90 kW, obtained in sec. 4.2, provide comparable intensities. (b) Normalized corrected spectral radiance of the object surface, $\tilde{L}_{\lambda}^{\text{corr}}$, for different time instants after injection. These are fitted with the normalized Planck distribution, $\tilde{L}_{\lambda}^{\text{bb}}(T)$, to provide the temperature T_{sp} . (c) Comparison between T_{sp} and the corrected apparent temperature from the two-color pyrometer, $T_{\text{app}}^{\text{corr}}$, show noticeable agreement.

6. Conclusions

Two-color ratio pyrometry provides powerful in situ diagnostics for plasma wind tunnel experiments of aerospace materials. However, the intense plasma radiation along the optical path poses a major concern for measurement accuracy.

In this work, we formulated a model of the instrument response that allowed a numerical assessment of the error. The gas spectral radiance was computed with

a radiation code, using temperature, pressure, and gas composition provided by CFD simulations of the plasma flow field. Our results show that gas radiation reaches a comparable intensity to the one emitted by the material for typical surface temperatures expected during PWT experiments. As a result, the measured signal ratio is shifted with respect to the value obtained during calibration, causing large positive errors in the measured temperature. The effect is particularly relevant during the transient heating phase of the material sample exposed to the plasma jet, while steady-state values appear negligibly affected.

A plasma wind tunnel test on a ceramic matrix composite material provided experimental data that confirmed the predicted trends, highlighting that a correction is necessary to improve the accuracy. Subtraction of reference signals, obtained right after the injection time, revealed a valuable procedure for a high-emittance material, as those could be interpreted as the contributions originating from the gas radiation only. A spectrometer, simultaneously pointed at the material, provided the spectral signature of either the gas and the surface, confirming the correction.

With the presented work, we provide a methodology to predict and understand an important biasing effect on ratio pyrometry, extending previous analyses concerning the influence of different environmental factors, and allowing experimentalists to achieve improved measurements in applications involving high-temperature gases. While a measurement correction is possible, future work should focus on identifying different wavelength ranges to minimize the interference of the plasma radiation. In this case, a compromise with the instrument's sensitivity needs to be accounted for. Additionally, while high-emittance materials allowed to neglect reflections from the surrounding gas, these could become important and would require further consideration in the case, for instance, of low-emittance metallic samples.

Acknowledgments

The research of A. Fagnani was funded by the Research Foundation - Flanders (dossier n. 1SB3121N). The experimental activities of this work were supported by the Air Force Office of Scientific Research (Grant N. FA9550-18-1-0209). V.Romano is acknowledged for the mesh convergence study on the CF-ICP code simulations. The authors would like to thank J. Freitas Monteiro for the precious help as Plasmatron test engineer and P. Collin as Plasmatron technical operator. S. Smolka, B.Bras and G.van Papendrecht are acknowledged for the support with the reflectometry measurements at the ESA ESTEC laboratories.

Declaration of Competing Interest

The authors declare that they have no known competing financial interests or personal relationships that could have appeared to influence the work reported in this paper.

References

- [1] J. D. J. Anderson, Hypersonic and High-Temperature Gas Dynamics, 2nd Edition, AIAA Education, 2006. doi:10.2514/4.861956.
- [2] G. Duffa, Ablative Thermal Protection Systems Modeling, American Institute of Aeronautics and Astronautics, Inc., Reston, Virginia, 2013. doi:10.2514/4.101717.
- [3] O. Chazot, F. Panerai, High-Enthalpy Facilities and Plasma Wind Tunnels for Aerothermodynamics Ground Testing, Hypersonic Nonequilibrium Flows: Fundamentals and Recent Advances (2015) 471–521doi:10.2514/5.9781624103292.0471.0522.
- [4] A. Turchi, J. J. Matesanz Saiz, T. E. Magin, O. Chazot, Duplication of hypersonic stagnation-region aerothermochemistry and gas-surface interaction in high-enthalpy ground testing, Experiments in Fluids 62 (11) (2021) 238. doi:10.1007/s00348-021-03320-6.
- [5] Gulhan A, Application of Pyrometry and IR-Thermography to High Surface Temperature Measurements, Tech. rep., NATO RTO (1999).
- [6] K. Chrzanowski, Problem of determination of effective emissivity of some materials in MIR range, Infrared Physics and Technology 36 (3) (1995) 679–684. doi:10.1016/1350-4495(94)00107-V.
- [7] A. Araujo, Multi-spectral pyrometry - A review, Measurement Science and Technology 28 (8) (2017) 082002. doi:10.1088/1361-6501/aa7b4b.
- [8] H. Huang, Z. Zhang, Y. Niu, C. Zhang, J. Jiang, Review of multispectral radiation thermometry data processing algorithms, Infrared Physics and Technology 129 (February) (2023) 104573. doi:10.1016/j.infrared.2023.104573.
- [9] Y. Zhang, Z. Zou, F. Yan, A multispectral thermometry based on multi-objective constraint optimization, Measurement: Journal of the International Measurement Confederation 192 (December 2021) (2022) 110813. doi:10.1016/j.measurement.2022.110813.

- [10] M. De Cesare, L. Savino, G. Ceglia, D. Alfano, F. Di Carlo, A. D. French, D. Rapagnani, S. Gravina, A. Cipullo, A. Del Vecchio, A. Di Leva, A. D’Onofrio, U. Galietti, L. Gialanella, F. Terrasi, Applied radiation physics techniques for diagnostic evaluation of the plasma wind and thermal protection system critical parameters in aerospace re-entry, *Progress in Aerospace Sciences* 112 (July 2019) (2020) 100550. doi:10.1016/j.paerosci.2019.06.001.
- [11] F. Panerai, O. Chazot, Characterization of gas/surface interactions for ceramic matrix composites in high enthalpy, low pressure air flow, *Materials Chemistry and Physics* 134 (2-3) (2012) 597–607. doi:10.1016/j.matchemphys.2012.03.036.
- [12] B. Helber, A. Turchi, J. B. Scoggins, A. Hubin, T. E. Magin, Experimental investigation of ablation and pyrolysis processes of carbon-phenolic ablators in atmospheric entry plasmas, *International Journal of Heat and Mass Transfer* 100 (2016) 810–824. doi:10.1016/j.ijheatmasstransfer.2016.04.072.
- [13] A. Fagnani, B. Helber, A. Hubin, O. Chazot, 3D infrared temperature maps measurements of ablative materials during plasma wind tunnel experiments, *Measurement Science and Technology* 34 (7) (2023) 075401. arXiv:0812.1538, doi:10.1088/1361-6501/acc67c.
- [14] F. S. Milos, Y. K. Chen, M. Mahzari, Arcjet tests and thermal response analysis for dual-layer woven carbon phenolic, *Journal of Spacecraft and Rockets* 55 (3) (2018) 712–722. doi:10.2514/1.A34142.
- [15] H. Böhrk, C. Dittert, H. Weihs, T. Thiele, A. Gülhan, Thermal testing of the sharp leading edge of SHEFEX II, 18th AIAA/3AF International Space Planes and Hypersonic Systems and Technologies Conference 2012 (September) (2012) 1–8. doi:10.2514/6.2012-5919.
- [16] L. Luo, Y. Wang, L. Duan, L. Liu, G. Wang, Ablation behavior of C/SiC-HfC composites in the plasma wind tunnel, *Journal of the European Ceramic Society* 36 (15) (2016) 3801–3807. doi:10.1016/j.jeurceramsoc.2016.03.017.
- [17] F. Zander, Surface temperature measurements in hypersonic testing using digital single-lens reflex cameras, *Journal of Thermophysics and Heat Transfer* 30 (4) (2016) 919–925. doi:10.2514/1.T4820.
- [18] R. Monier, F. Thumerel, J. Chapuis, F. Soulié, C. Bordreuil, Liquid metals surface temperature fields measurements with a two-colour pyrometer,

Measurement: Journal of the International Measurement Confederation 101 (2017) 72–80. doi:10.1016/j.measurement.2016.12.031.

- [19] M. Musto, G. Rotondo, M. De Cesare, A. Del Vecchio, L. Savino, F. De Filippis, Error analysis on measurement temperature by means dual-color thermography technique, Measurement 90 (2016) 265–277. doi:10.1016/j.measurement.2016.04.024.
- [20] L. Savino, A. Martucci, A. Del Vecchio, M. De Cesare, A novel physics methodology based on compact emission spectroscopy in the VNIR (0.4–0.9 μm) ranges for plasma shock layer/material temperature determinations and surface emissivity evaluations in the VNIR – LWIR (7–14 μm) ranges during atmospheric re-entr, Infrared Physics and Technology 108 (May) (2020) 103353. doi:10.1016/j.infrared.2020.103353.
- [21] F. Di Carolo, L. Savino, D. Palumbo, A. Del Vecchio, U. Galietti, M. De Cesare, Standard thermography vs free emissivity dual color novel CIRA physics technique in the near-mid IR ranges: Studies for different emissivity class materials from low to high temperatures typical of aerospace re-entry, International Journal of Thermal Sciences 147 (September 2019) (2020) 106123. doi:10.1016/j.ijthermalsci.2019.106123.
- [22] T. Yu, F. J. Bauer, F. J. Huber, S. Will, W. Cai, 4D temperature measurements using tomographic two-color pyrometry, Optics Express 29 (4) (2021) 5304. doi:10.1364/oe.412821.
- [23] A. S. Tenney, Radiation Ratio Thermometry, in: Theory and Practice of Radiation Thermometry, John Wiley & Sons, Inc., Hoboken, NJ, USA, pp. 459–494. doi:10.1002/9780470172575.ch6.
- [24] C. Rodiet, B. Remy, A. Degiovanni, Optimal wavelengths obtained from laws analogous to the Wien’s law for monospectral and bispectral methods, and general methodology for multispectral temperature measurements taking into account global transfer function including non-uniform emissivity of, Infrared Physics and Technology 76 (2016) 444–454. doi:10.1016/j.infrared.2016.04.006.
- [25] Y. Huang, M. Long, J. Zhao, H. Fan, D. Chen, K. Tan, H. Duan, Coupled effects of reflection and absorptive gas mixture on surface temperature determined by single color pyrometer, Journal of Quantitative Spectroscopy and Radiative Transfer 228 (2019) 111–123. doi:10.1016/j.jqsrt.2019.02.022.

- [26] A. Tapetado, J. Diaz-Alvarez, M. H. Miguelez, C. Vazquez, Two-color pyrometer for process temperature measurement during machining, *Journal of Lightwave Technology* 34 (4) (2016) 1380–1386. doi:10.1109/JLT.2015.2513158.
- [27] D. Ketui, F. Chi, G. Shan, Single wavelength and ratio pyrometry reflection errors in temperature measurement of gas turbine blade, *Measurement: Journal of the International Measurement Confederation* 86 (2016) 133–140. doi:10.1016/j.measurement.2016.02.054.
- [28] P. Saunders, Reflection errors and uncertainties for dual and multiwavelength pyrometers, *High Temperatures - High Pressures* 32 (2) (2000) 239–249. doi:10.1068/htrt201.
- [29] D. Lowe, G. Machin, M. Sadli, Correction of temperature errors due to the unknown effect of window transmission on ratio pyrometers using an in situ calibration standard, *Measurement: Journal of the International Measurement Confederation* 68 (2015) 16–21. doi:10.1016/j.measurement.2015.02.043.
- [30] V. Mlačnik, I. Pušnik, Influence of atmosphere on calibration of radiation thermometers, *Sensors* 21 (16) (2021). doi:10.3390/s21165509.
- [31] A. Araújo, Dual-band pyrometry for emissivity and temperature measurements of gray surfaces at ambient temperature: The effect of pyrometer and background temperature uncertainties, *Measurement: Journal of the International Measurement Confederation* 94 (2016) 316–325. doi:10.1016/j.measurement.2016.08.007.
- [32] C. O. Laux, T. G. Spence, C. H. Kruger, R. N. Zare, Optical diagnostics of atmospheric pressure air plasmas, *Plasma Sources Science and Technology* 12 (2) (2003) 125–138. doi:10.1088/0963-0252/12/2/301.
- [33] A. Fagnani, D. Le Quang Huy, B. Helber, S. Demange, A. Turchi, O. Chazot, A. Hubin, Investigation of a Free-Stream Air Plasma Flow by Optical Emission Spectroscopy and Comparison to Magnetohydrodynamics Simulations, in: *AIAA Scitech 2020 Forum*, no. January, American Institute of Aeronautics and Astronautics, Reston, Virginia, 2020, pp. 1–15. doi:10.2514/6.2020-0382.
- [34] O. R. Loesener, M. Auweter-Kurtz, M. Hartling, E. W. Messerschmid, Linear pyrometer for investigations of thermal protection systems, *Journal of Thermophysics and Heat Transfer* 7 (1) (1993) 82–87. doi:10.2514/3.11573.

- [35] O. Loesener, G. Neuer, A new far-infrared pyrometer for radiation temperature measurement on semitransparent and absorbing materials in an arc-heated wind tunnel, *Measurement* 14 (2) (1994) 125–134. doi:10.1016/0263-2241(94)90021-3.
- [36] M. E. MacDonald, C. M. Jacobs, C. O. Laux, F. Zander, R. G. Morgan, Measurements of air plasma/ablator interactions in an inductively coupled plasma torch, *Journal of Thermophysics and Heat Transfer* 29 (1) (2015) 12–23. doi:10.2514/1.T4402.
- [37] T. Sakuta, M. I. Boulos, Novel approach for particle velocity and size measurement under plasma conditions, *Review of Scientific Instruments* 59 (2) (1988) 285–291. doi:10.1063/1.1140242.
- [38] P. Gougeon, C. Moreau, In-flight particle surface temperature measurement: Influence of the plasma light scattered by the particles, *Journal of Thermal Spray Technology* 2 (3) (1993) 229–233. doi:10.1007/BF02650470.
- [39] Z. Salhi, P. Gougeon, D. Klein, C. Coddet, Influence of plasma light scattered by in-flight particle on the measured temperature by high speed pyrometry, *Infrared Physics and Technology* 46 (5) (2005) 394–399. doi:10.1016/j.infrared.2004.07.001.
- [40] B. Aziz, P. Gougeon, C. Moreau, Temperature Measurement Challenges and Limitations for In-Flight Particles in Suspension Plasma Spraying, *Journal of Thermal Spray Technology* 26 (4) (2017) 695–707. doi:10.1007/s11666-017-0543-8.
- [41] C. L. Wyatt, *Radiometric Calibration: Theory and Methods*, Elsevier, 1978. doi:10.1016/b978-0-12-766150-6.x5001-4.
- [42] G. D. Nutter, Radiation Thermometers: Design Principles and Operating Characteristics, in: *Theory and Practice of Radiation Thermometry*, John Wiley & Sons, Inc., Hoboken, NJ, USA, pp. 231–337. doi:10.1002/9780470172575.ch4.
- [43] Michael F Modest, *Radiative Heat Transfer*, Elsevier, 2013. doi:10.1016/C2010-0-65874-3.
URL <https://linkinghub.elsevier.com/retrieve/pii/C20100658743>
- [44] B. Bottin, Aerothermodynamic model of an Inductively-Coupled Plasma Wind Tunnel, Ph.D. thesis, von Karman Institute for Fluid Dynamics & Université de Liège (1999).

- [45] B. Bottin, M. Carbonaro, S. Zemsch, G. Degrez, B. Bottin, M. Carbonaro, S. Zemsch, G. Degrez, Aerothermodynamic design of an inductively coupled plasma wind tunnel, in: 32nd Thermophysics Conference, no. July, American Institute of Aeronautics and Astronautics, Reston, Virginia, 1997. doi:10.2514/6.1997-2498.
- [46] B. Bottin, S. Paris, V. Van Der Haegen, M. Carbonaro, Experimental and computational determination of the VKI Plasmatron operating envelope, in: 30th Plasmadynamic and Lasers Conference, no. c, American Institute of Aeronautics and Astronautics, Reston, Virginia, 1999. doi:10.2514/6.1999-3607.
- [47] H.-J. Kunze, Introduction to Plasma Spectroscopy, Vol. 56 of Springer Series on Atomic, Optical, and Plasma Physics, Springer Berlin Heidelberg, Berlin, Heidelberg, 2009. doi:10.1007/978-3-642-02233-3.
- [48] G. Degrez, D. V. Abeele, P. Barbante, B. Bottin, Numerical simulation of inductively coupled plasma flows under chemical non-equilibrium, International Journal of Numerical Methods for Heat and Fluid Flow 14 (4) (2004) 538–558. doi:10.1108/09615530410532286.
- [49] A. Lani, N. Villedieu, K. Bensassi, L. Kapa, M. Vymazal, M. S. Yalim, M. Panesi, COOLFluid: An open computational platform for multi-physics simulation and research, 21st AIAA Computational Fluid Dynamics Conference (2013) 1–25doi:10.2514/6.2013-2589.
- [50] J. B. Scoggins, V. Leroy, G. Bellas-Chatzigeorgis, B. Dias, T. E. Magin, Mutation++: MUlticomponent Thermodynamic And Transport properties for IONized gases in C++, SoftwareX 12 (2020). arXiv:2002.01783, doi:10.1016/j.softx.2020.100575.
- [51] T. Magin, A Model for Inductive Plasma Wind Tunnels, Ph.D. thesis, von Karman Institute for Fluid Dynamics & Université libre de Bruxelles (2004).
- [52] B. A. Cruden, A. M. Brandis, Updates to the NEQAIR radiation solver, in: International Workshop on Radiation in High Temperature Gases, 2014.
- [53] Non-Equilibrium Air Radiation (NEQAIR) code.
URL <https://software.nasa.gov/software/ARC-15262-1B>